H&E-stained Whole Slide Image Deep Learning Predicts SPOP Mutation State in Prostate Cancer

Andrew J. Schaumberg[a,b,*], **Mark A. Rubin**[c,d,e,*], **and Thomas J. Fuchs**[f,g,*]

[a]Memorial Sloan Kettering Cancer Center and the Tri-Institutional Training Program in Computational Biology and Medicine; [b]Weill Cornell Graduate School of Medical Sciences; [c]Caryl and Israel Englander Institute for Precision Medicine, New York Presbyterian Hospital–Weill Cornell Medicine; [d]Sandra and Edward Meyer Cancer Center at Weill Cornell Medicine; [e]Department of Pathology and Laboratory Medicine, Weill Cornell Medicine; [f]Department of Medical Physics, Memorial Sloan Kettering Cancer Center; [g]Department of Pathology, Memorial Sloan Kettering Cancer Center

This manuscript was compiled on March 3, 2017

A quantitative model to genetically interpret the histology in whole microscopy slide images is desirable to guide downstream immunohistochemistry, genomics, and precision medicine. We constructed a statistical model that predicts whether or not SPOP is mutated in prostate cancer, given only the digital whole slide after standard hematoxylin and eosin [H&E] staining. Using a TCGA cohort of 177 prostate cancer patients where 20 had mutant SPOP, we trained multiple ensembles of residual networks, accurately distinguishing SPOP mutant from SPOP wild type patients. We further validated our full metaensemble classifier on an independent test cohort from MSK-IMPACT of 152 patients where 19 had mutant SPOP. Mutants and non-mutants were accurately distinguished despite TCGA slides being frozen sections and MSK-IMPACT slides being formalin-fixed paraffin-embedded sections. Importantly, our method demonstrates tractable deep learning in this "small data" setting of 20 positive examples. To our knowledge, this is the first statistical model to predict a genetic mutation in cancer directly from the patient's digitized H&E-stained whole microscope slide.

cancer | molecular pathology | deep learning | whole slide image

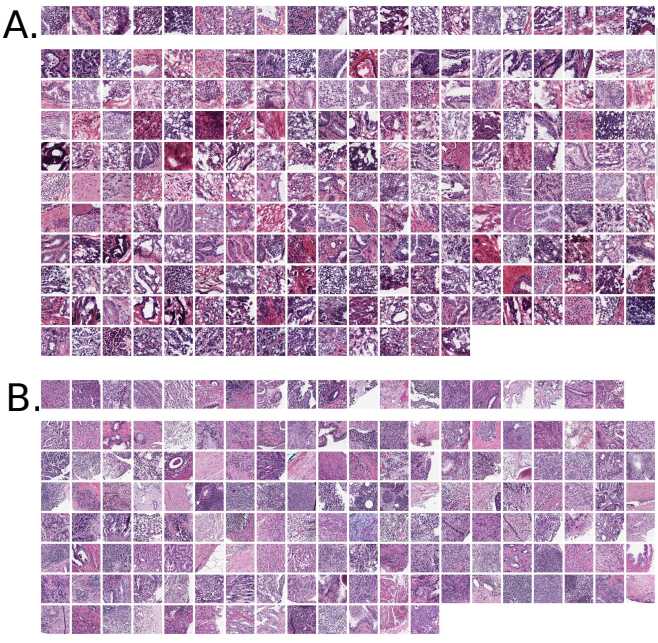

Fig. 1. *Panel A:* TCGA cohort. Top row shows 20 SPOP mutants. Remaining below are 157 SPOP wild type patients, where 25 patients had 2 and 6 patients had 3 acceptable slides available. Images are frozen sections. *Panel B:* MSK-IMPACT cohort. Top row shows 19 SPOP mutants. Remaining below are 133 SPOP wild type patients. Images are formalin-fixed paraffin-embedded sections, which provide higher image quality than frozen sections.

Genetic drivers of cancer morphology, such as E-Cadherin [CDH1] loss promoting lobular rather than ductal phenotypes in breast, are well known. SPOP mutation in prostate cancer has a number of known morphological traits, including blue-tinged mucin, cribriform pattern, and macronuclei [5]. Computational pathology methods [6] typically predict clinical or genetic features as a function of histological imagery, e.g. whole slide images. Our central hypothesis is that the morphology shown in these whole slide images, having nothing more than standard hematoxylin and eosin [H&E] staining, is a function of the underlying genetic drivers. To test this hypothesis, we gathered a cohort of 499 prostate adenocarcinoma patients from The Cancer Genome Atlas [TCGA][1], 177 of which were suitable for analysis, with 20 of those having mutant SPOP (Figs 1, 2, and 3). We then used ensembles of deep convolutional neural networks to accurately predict whether or not SPOP was mutated in the patient, given only the patient's whole slide image (Figs 4 and 5), leveraging spatial localization of SPOP mutation evidence in the histology imagery for statistically significant SPOP mutation prediction accuracy when training on TCGA but testing on MSK-IMPACT[7] cohorts (Figs 6 and 7). Our classifier's generalization error bounds (Fig 7, panel A, second from right), receiver operating characteristic (Fig 7, panel B6), and independent dataset performance (Fig 7, panel C1) support our hypothesis, in agreement with

Significance Statement

The authors present the first automatic pipeline predicting gene mutation probability in cancer from digitized light microscopy slides having standard hematoxylin and eosin staining. To predict whether or not the speckle-type POZ protein [SPOP] gene is mutated in prostate cancer, the pipeline (i) identifies diagnostically salient regions in the whole slide at low magnification, (ii) identifies the salient region having the dominant tumor, (iii) within this region finds the high magnification subregion most enriched for abnormal cells, and (iv) trains ensembles of deep learning binary classifiers that together predict a confidence interval of mutation probability. Through deep learning on small datasets, this work enables fully-automated histologic diagnoses based on probabilities of underlying molecular aberrations. Such probabilities may directly guide immunohistochemistry choices, genetic tests, and precision medicine.

Conception, Writing: AJS, TJF. Algorithms, Learning: AJS. Analysis: AJS, MAR, TJF. Supervision: MAR, TJF.

Authors declare no conflicts of interest.

*To whom correspondence should be addressed. E-mail: ajs625@cornell.edu, rubinma@med.cornell.edu, fuchst@mskcc.org

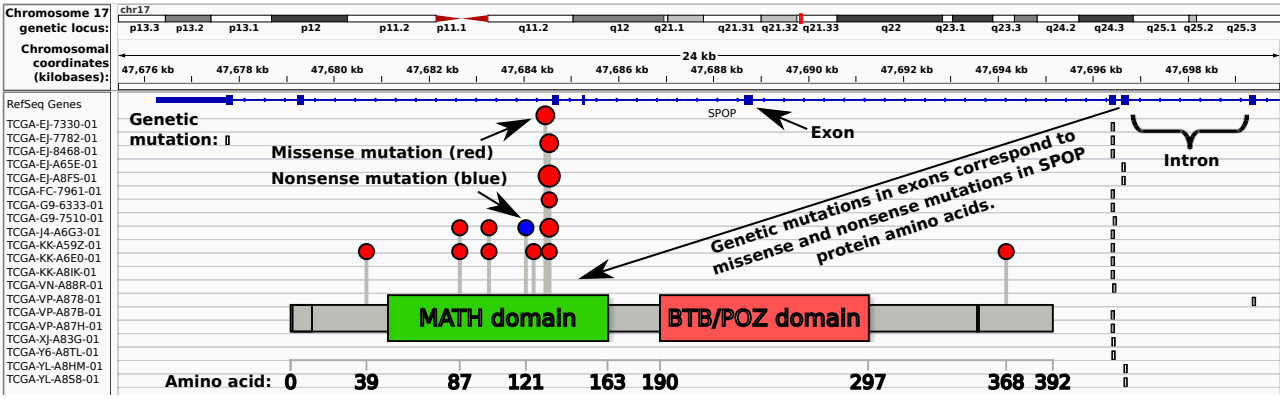

Fig. 2. SPOP mutations in the Integrated Genomics Viewer [1, 2], with lollipop plot showing mutations in most frequently mutated domain. For two of twenty patients, somatic SPOP mutations fall outside the MATH domain, responsible for recruiting substrates for ubiquitinylation.

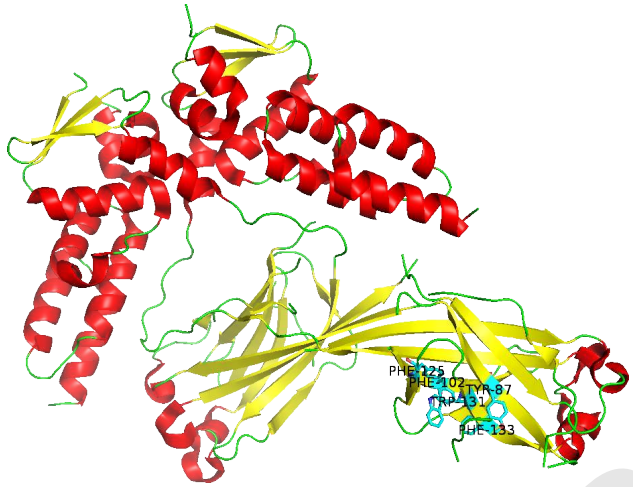

Fig. 3. SPOP tertiary structure with mutated residues labeled, common to one site. Though most genetic aberrations affect a single Cullin-3 [CUL3] binding pocket in SPOP, our method's performance appears robust to two of 20 patients having genetic changes outside this pocket. Mutation chr17:47677762 R368H in patient TCGA-EJ-7782-01 not shown and not in site. Deletion chr17:47699392 in patient TCGA-VP-A878 not shown and not in site. PDB structure 3HQI.

earlier work suggesting SPOP mutants are a distinct subtype of prostate cancer [8].

Previously, pathologists described slide image morphologies, which were then correlated to molecular aberrations, such as mutations and copy number alterations [9, 10]. Our deep learning approach instead learns features from the images without a pathologist, using a single mutation as a class label, and quantifies prediction uncertainty through confidence intervals [CIs] (Fig 4).

Others used support vector machine techniques to predict molecular subtypes in a bag-of-features approach over Gabor filters [11]. The authors avoided deep learning due to limited data available. Gabor filters resemble first layer features in a convolutional network. A main contribution of ours is using pre-training, Monte Carlo cross validation, and heterogeneous ensembles to enable deep learning despite limited data. We believe our method's prediction of a single mutation is more clinically actionable than predicting broad gene expression subtypes.

[1] TCGA data courtesy the TCGA Research Network http://cancergenome.nih.gov/

Support vector machines, Gaussian mixture modeling, and principal component analyses have predicted PTEN deletion and copy number variation in cancer, but relied on fluorescence *in situ* hybridization [FISH], a very specific stain [12]. Our approach uses standard H&E, a non-specific stain that we believe could be utilized to predict more molecular aberrations than only the SPOP mutation that is our focus here. However, our method does not quantify tumor heterogeneity.

Tumor heterogeneity has been analyzed statistically by other groups [13], as a spatial analysis of cell type entropy cluster counts in H&E-stained whole slides. A high count, when combined with genetic mutations such as TP53, improves patient survival prediction. This count is shown to be independent of underlying genetic characteristics, whereas our method predicts a genetic characteristic, i.e. SPOP mutation, from convolutional features of the imaging.

Histological review to identify patients having a specific genetic mutation for the development of targeted inhibitors has been previously proposed in the context of fibroblast growth factor receptor 3 [FGFR3] and CDH1 mutations in bladder cancer [14, 15]. FGFR3 mutants revealed unique histological features, this represents a potential therapeutic target, and follow-up confirmatory genotyping is suggested. Our approach with SPOP mutants in prostate cancer is similar, with deep learning ensembles in place of pathologists to analyze the slide.

Results

Molecular information as labels of pathology images opens a new field of molecular pathology. Rather than correlating or combining genetic and histologic data, we predict a gene mutation directly from a whole slide image having unbiased H&E staining. This not only enables systematic investigation of other genotype and phenotype relationships on the basis of deep learning models such as ours, but serves as a new supervised learning paradigm for clinically actionable molecular targets, independent of clinician-supplied labels of the histology. Epigenetic, copy number alteration, gene expression, and post-translational modification data may all be brought to bear as labels for histology. Deep learning ensemble approaches such as ours may then learn to predict these labels from images. Future work may refine these predictions to single-cell resolution, combined with single-cell sequencing, immunohistochemistry, fluorescence *in situ* hybridization, mass

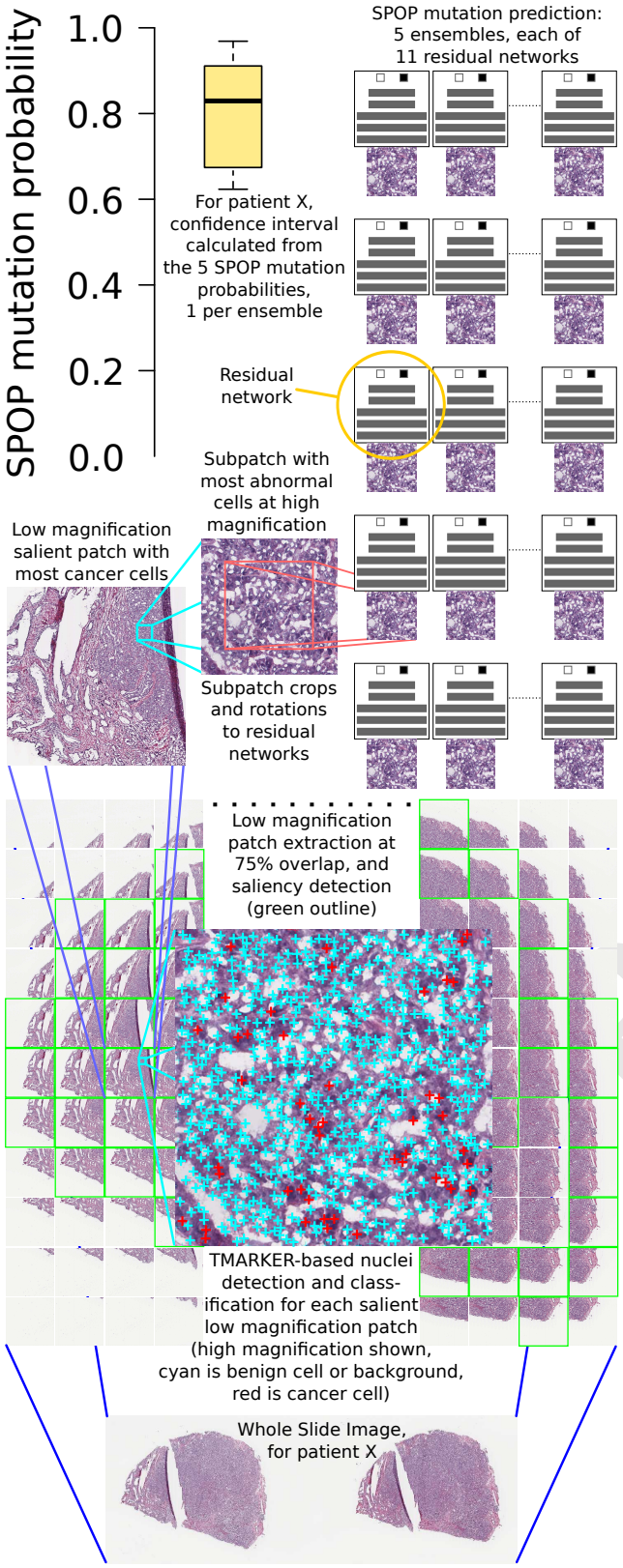

Fig. 4. Pipeline: a whole slide image is split into patches (bottom) at low magnification. Salient patches are identified. The salient patch with the most cancer cells is deemed the "dominant tumor" patch and further analyzed. At high magnification, a sliding window within the dominant tumor patch finds the region with maximum abnormal cells. Deep neural networks then predict SPOP mutation and a confidence interval is calculated over these predictions.

cytometry[16], or other technologies to label corresponding H&E images or regions therein. We suggest focusing on labels that are clinically actionable, such as gains or losses of function. Soon we hope to interpret our deep network's predictions through DeepVis or a similar tool [17].

SPOP mutation state prediction is learnable from a small set of whole slides stained with hematoxylin and eosin. Despite SPOP being one of the most frequently mutated genes in prostate adenocarcinomas, from a TCGA cohort of 499 patients only 177 passed our quality control and only 20 of these had SPOP mutation. Meanwhile in the 152-patient MSK-IMPACT cohort there were only 19 SPOP mutants, indicating that there are difficulties in practice acquiring large cohorts of patients with both quality whole slide cancer pathology images and genetic sequencing represented. This challenge increases for rare genetic variants. Moreover, different cohorts may have different slide preparations and appearances, such as TCGA being frozen sections and MSK-IMPACT being higher quality formalin-fixed paraffin embedded sections (Fig 1). Nonetheless, our pipeline (Fig 4) accurately predicts whether or not SPOP is mutated in the MSK-IMPACT cohort when trained on the TCGA cohort (Fig 7). We leverage pre-trained neural networks, Monte Carlo cross validation, class-balanced stratified sampling, and architecturally hetergeneous ensembles for deep learning in this "small data" setting of only 20 positive examples, which may remain relevant for rare variants as more patient histologies and sequences become available in the future. To our knowledge this is the first time a mutation in cancer has been predicted through deep learning on whole slides with standard H&E staining.

SPOP mutation state prediction is accurate and the prediction uncertainty is bounded within a confidence interval. Our pipeline's accuracy in SPOP mutation state prediction is statistically significant, both within held-out test datasets in TCGA and against the indepdendent MSK-IMPACT cohort (Fig 7). The confidence interval [CI] calculated using five ResNet ensembles allows every prediction to be evaluated statistically: is there significant evidence for SPOP mutation in the patient, is there significant evidence for SPOP wild type in the patient, or is the patient's SPOP mutation state inconclusive. Clinicians may choose to follow the mutation prediction only if the histological imagery provides acceptably low uncertainty.

SPOP mutation state prediction is fully automated and does not rely on human interpretation. Unlike Gleason score, which relies on a clinician's interpretation of the histology, our pipeline is fully automated (Fig 4). The pipeline's input is the whole digital slide and the output is the SPOP mutation prediction bounded within 95% and 99% CIs. Moreover, our pipeline does not require a human to identify a representative region in the slide, as is done to create tissue microarrays [TMAs] from slides.

Molecular pathology, such as characterizing histology in terms of SPOP mutation state, leads directly to precision medicine. For instance, wild type SPOP ubiquitinylates androgen receptor [AR], to mark AR for degradation, but mutant SPOP does not. Antiandrogen drugs, such as flutamide, promote degradation of AR to treat the cancer, though mutant AR confers resistance [18, 19].

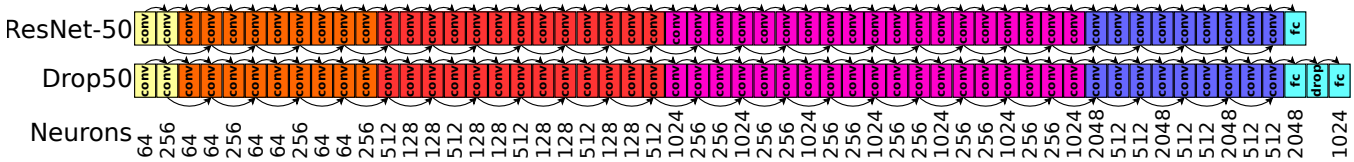

Fig. 5. ResNet-50 architecture [3], top. Customized Drop50 architecture supports ResNet-50 pretraining, but has additional dropout [4] and fully connected neuron layers. In practice at least one of these architectures converges to a validation accuracy of 0.6 or more. Convolutional layers "conv", fully-connected layers "fc", 50% dropout layer "drop". ResNet-50 has 26,560 neurons and Drop50 has 28,574. All five trials, each trial being a multiarchitectural ensemble of eleven residual networks, is 1,491,012 neurons total.

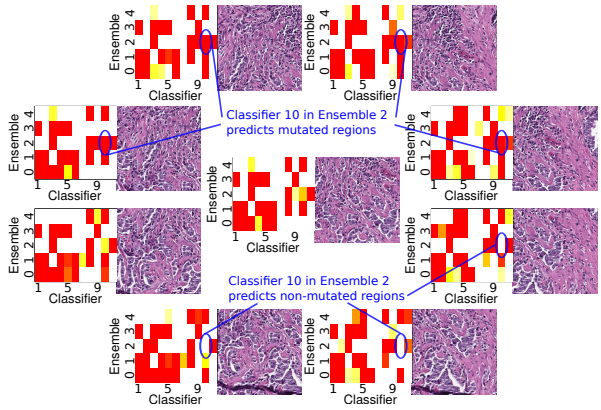

Fig. 6. Region of interest and surrounding octagon patches. Overall classifier prediction is weighted by nine-patch prediction variance, so ensemble 2 predicts SPOP is mutated (0.6292 mean ensemble prediction, 0.5093-0.7790 95% CI, 0.4908-0.8147 99% CI).

SPOP mutation state prediction provides information regarding other molecular states. SPOP mutation is mutually exclusive with TMPRSS2-ERG gene fusion [8], so our SPOP mutation predictor provides indirect information regarding the TMPRSS2-ERG state and potentially others.

Discussion

In this work, we summarize a whole histology slide with a maximally abnormal subregion within the dominant tumor, such that the vast majority of the slide is not used for deep learning. Tissue microarrays take a similar although manual approach, by using a small representative circle of tissue to characterize a patient's cancer. In a sense, our patch extraction, saliency prediction, and TMARKER-based cell counting pipeline stages together model how a representative patch may be selected to identify the dominant cancer subtype in the slide overall, ignoring other regions that may not have the same genetic drivers. By using a high magnification abnormal subregion, we aim to capture cellular-level image features driven by the dominant underlying molecular change, such as SPOP mutation. This subregion has many desirable properties:

1. it is salient at low magnification, i.e. diagnostically relevant to a pathologist when making a diagnosis at the microscope [20],

2. it has the maximum number of malignant cells at low magnification, which is a heuristic to locate the dominant tumor, presumably enriched for cells with driver mutations such as SPOP due to conferred growth advantages,

3. it has the maximum number of abnormal cells at high magnification, which is a heuristic to locate a subregion with most nuanced cellular appearance, presumably concentrated with cellular-level visual features that can discriminate between cancers driven by SPOP versus other mutations, and

4. it is large enough at high magnification to capture histology, such as gland structure in this 800x800 pixel [px] patch.

A holistic approach that considers for deep learning patches spatially distributed widely throughout the slide, rather than only the dominant tumor, could improve performance and provide further insight. Gleason grading involves such a holistic approach, identifying first and second most prevalent cancer morphologies in a whole slide. We leave for future work the complexities of multiple representatives per slide, varying numbers of representatives per slide, and considering simultaneously multiple slides per patient.

Rather than use a single classifier, we use multiple classifier ensembles to predict the SPOP mutation state. Though each residual network [3] classifier tends to predict SPOP mutation probability in a bimodal distribution, i.e. being either close to 0 or close to 1, averaging these classifiers within an ensemble provides a uniform distribution representing the SPOP mutation probability (Fig S1).

Deep learning typically requires large sets of training data, yet we have only 20 patients with SPOP mutation, nearly an order of magnitude fewer than the 157 patients without somatic SPOP mutation in the TCGA cohort. Deep learning in small data is a challenging setting. Our metaensemble approach confronts this challenge by training many residual networks [ResNets] on small draws of the data, in equal proportions of SPOP mutants and SPOP wild type, then combining the ResNets as weak learners, to produce a strong learner ensemble [21, 22], similar in principle to a random forest ensemble of decision trees [23]. Empirically, the great depth of ResNets appears to be important because CaffeNet [24] – a shallower 8-layer neural network based on AlexNet [25] – rarely achieved validation accuracy of 0.6 or more predicting SPOP mutation state.

Pretraining the deep networks is essential in small data regimes such as ours, and we use the ResNet-50 model pretrained on ImageNet [3]. We used both the published ResNet-50 and our customized ResNet-50 that included an additional 50% dropout [4] layer and a 1024-neuron fully-connected layer. In practice, for difficult training set draws, at least one of these architectures would often converge to validation accuracy of 0.6 or more. For data augmentation, the 800x800px images at high magnification are trimmed to the centermost 512x512px in 6 degree rotations, scaled to 256x256px, flipped and unflipped, then randomly cropped to 224x224 within Caffe [24] for training. Learning rates varied from 0.001 to 0.007,

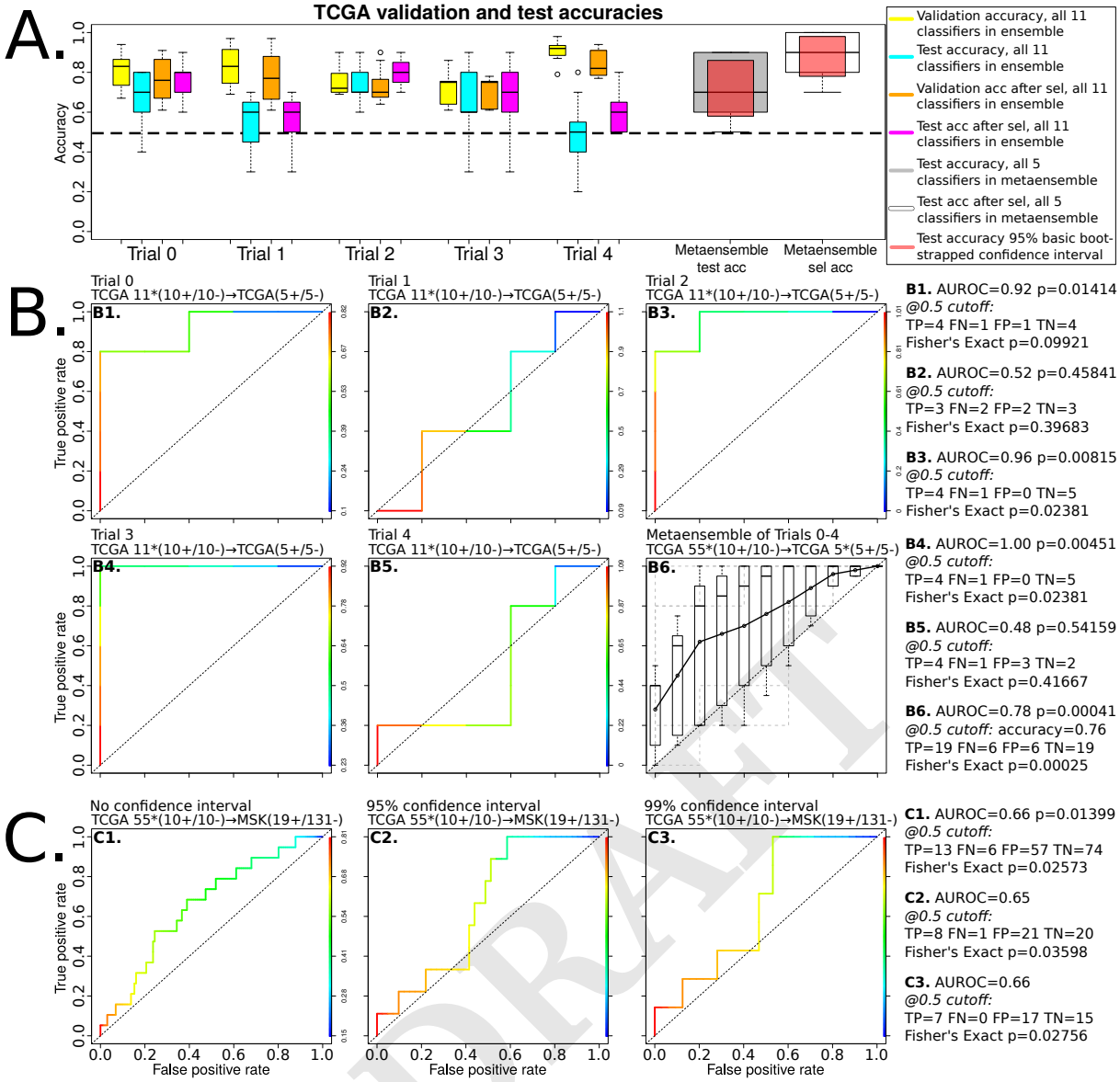

Fig. 7. Stricter CIs reduce false negatives and maintain significant Fisher's Exact p-values, but ignore more predictions as inconclusive (panel C and Alg S3). This performance ($0.01 < p < 0.05$, panel C) is expected due to only 20 SPOP mutants in TCGA dataset, and that TCGA is frozen sections while MSK-IMPACT is fixed sections (Fig 1).

and momentums from 0.3 to 0.99. Test error tended to be worse with momentum less than 0.8, though low momentum allowed convergence for difficult training sets. Learning rates of 0.001, 0.0015, or 0.002 with momentum of 0.9 was typical. We used nVidia Titan-X GPUs with 12GB RAM for training. At 12GB, one GPU could train either ResNet architecture using a minibatch size of 32 images.

Materials and Methods

Digital slide acquisition and quality control: TCGA slides and SPOP mutation state was downloaded from cBioPortal [26]. The MSK-IMPACT cohort was available internally. We discarded slide regions that were not diagnostically salient [20]. We discarded slide regions that were (i) over-stained eosin blue, (ii) > 50% erythrocytes, (iii) > 50% empty, or (iv) > 50% blurred, by inspection (Alg S1). Patients having no regions remaining were discarded. A region is a 800x800 pixel [px] patch at 8 microns per pixel [μpp], ~100x magnification.

Region of interest identification: For each region, we used TMARKER[27] to identify cell nuclei and classify them as benign, malignant, or unknown – using a corresponding 12750x12750px patch at level 0 of the slide SVS file (0.25 μpp) for the 800x800px region passing quality control (Fig 4). The 12750x12750px patch having the most malignant cells in this slide was deemed the "dominant tumor" after searching in a 10px grid for an 800x800px region of interest patch (at 4 μpp) having maximal abnormal cells. A malignant cell is 1 abnormal cell while an unknown cell is 0.5 abnormal cell and 0.5 normal cell. We expected a mutant driver gene, such as SPOP, to confer a growth advantage evident in the region of interest and show histological features, such as ducts. By maximizing abnormal cell counts, we intended to find as many discriminative image textures based on SPOP-mutation-driven cancer cells as possible.

Data augmentation: In an 800x800px region of interest patch, the centermost 512x512px patch was selected, rotated in six degree increments for rotational invariance, and scaled to 256x256px. Eight 800x800px patches were also selected in a surrounding octagon formation around the region of interest, offset 115 and 200px away from the central region of interest, so two adjacent octagon patches were

230px away from each other and 230px away from the central patch (Fig 6). These patches were rotated and scaled. This integrates a circular area to summarize the slide, akin to circular tissue cuts in TMAs.

Deep learning: We used Caffe [24] for deep learning a binary classification model given the 256x256px patches labeled by SPOP mutation state. We adapted the ResNet-50 [3] model pre-trained on ImageNet [28] data by re-initializing the last layer's weights (Fig 5), then trained on pathology images. Classifier predictions followed a sharply bimodal distribution of 0 or 1, but ensemble predictions followed a uniform distribution suitable for CIs (Fig S1).

Experiments

Cross validation: For a trial, a test set of 5 positive and 5 negative [5+/5-] examples was used, where a positive example is a patient with SPOP mutation (Table S1). If a patient had multiple slides that passed quality control, at most one was used in the trial, taken at random. With the test set held out, we ran Monte Carlo cross validation 13 times, each time (i) drawing without replacement a training set of 10+/10- examples and validation set of 5+/5- examples, and (ii) training both a ResNet-50 and Drop50 classifier (Fig 5). Our convergence criterion was classifier validation accuracy $>= 0.6$ with $10000 - 100000$ training iterations. An ensemble was 11 classifiers, one per Monte Carlo cross validation, allowing 2 of 13 Monte Carlo cross validation runs to converge poorly or not at all (Alg S2). Empirically, this class-balanced stratified-sampling ensemble approach reduces classifier bias towards the majority class and broadly samples both classes.

Ensemble aggregation: To estimate generalization error, the 11 classifiers in a trial were selected by highest validation accuracy to form an ensemble, and a metaensemble from 5 independent trial ensembles. A 95% basic bootstrapped CI[2] indicated generalization accuracy from these 5 trials was 0.58-0.86 – significantly better than 0.5 chance (Fig 7, panel A, second from right). Metaensemble AUROC was 0.78 (p=0.00041), accuracy was 0.76, and Fisher's Exact Test p=0.00025 – indicating the method performs significantly better than chance on unseen data (Fig 7, panel B6). We formed tuned ensembles (Fig S2), where 11 classifiers in a trial were selected by highest ensemble *test* accuracy, which no longer estimates generalization error but promotes correct classification on average across ensembled classifiers for each test example (Fig 7, panel A, white versus gray).

Independent evaluation: We tested the metaensemble of 5 tuned 11-classifier ensembles on the MSK-IMPACT cohort. Each patient had one slide. For each slide, a central region of interest and surrounding octagon of patches were found, for nine patches per slide (Fig 6). We hypothesized that SPOP mutation leads to 1-2 nine-patch-localized lesions, meaning adjacent patches have similar classifier-predicted SPOP mutation probability. So, of the nine patches we formed all possible groups of three adjacent patches and assigned to a group the minimum SPOP mutation probability of any patch in the grouped three, then took the second-greatest group as a classifier's overall patient cancer mutation prediction. Within an ensemble, we weighted a classifier's overall prediction by the classifier's nine-patch mutation prediction variance, because classifiers with high variance (e.g. mostly mutant, but 1-3 of nine non-mutant) reflect the lesion hypothesis better than classifiers that predict all non-mutant (0) or all mutant (1). Thus on MSK-IMPACT, the metaensemble assigned stochastically greater scores to mutants than non-mutants (AUROC 0.66, p=0.01399) and accurately distinguished mutants from non-mutants (Fisher's Exact p=0.02573) (Fig 7, panel C1). This is consistent with generalization accuracy 95% CI significance (Fig 7, panel A, second from right) and test AUROC of 0.78 (Fig 7, panel B6) within TCGA.

[2] We used the R `boot` library for basic bootstrap CIs. Canty and Ripley 2016: https://cran.r-project.org/web/packages/boot/index.html

ACKNOWLEDGMENTS. AJS was supported the Tri-Institutional Training Program in Computational Biology and Medicine (via NIH training grant T32GM083937). This research was funded in part through the NIH/NCI Cancer Center Support Grant P30CA008748. We gratefully acknowledge GPU support from NVIDIA corporation as part of a GPU Research Center award to TJF. AJS and TJF were supported by MSK Functional Genomics Initiative grant to TJF.

References

1. Thorvaldsdóttir H, Robinson J, Mesirov J (2013) Integrative Genomics Viewer (IGV): high-performance genomics data visualization and exploration. *Briefings in Bioinformatics* 14(2):178–192.
2. Robinson J et al. (2011) Integrative genomics viewer. *Nature Biotechnology* 29(1):24–26.
3. He K, Zhang X, Ren S, Sun J (2015) Deep Residual Learning for Image Recognition.
4. Srivastava N, Hinton G, Krizhevsky A, Sutskever I, Salakhutdinov R (2014) Dropout: A Simple Way to Prevent Neural Networks from Overfitting. Vol. 15, pp. 1929–1958.
5. Mosquera JM et al. (2007) Morphological features of TMPRSS2-ERG gene fusion prostate cancer. *The Journal of pathology* 212(1):91–101.
6. Fuchs T, Buhmann J (2011) Computational pathology: challenges and promises for tissue analysis. *Computerized medical imaging and graphics : the official journal of the Computerized Medical Imaging Society* 35(7-8):515–530.
7. Cheng D et al. (2015) Memorial Sloan Kettering-Integrated Mutation Profiling of Actionable Cancer Targets (MSK-IMPACT): A Hybridization Capture-Based Next-Generation Sequencing Clinical Assay for Solid Tumor Molecular Oncology. *The Journal of molecular diagnostics : JMD* 17(3):251–264.
8. Barbieri C et al. (2012) Exome sequencing identifies recurrent SPOP, FOXA1 and MED12 mutations in prostate cancer. *Nature Genetics* 44(6):685–689.
9. Hakimi A et al. (2015) TCEB1-mutated renal cell carcinoma: a distinct genomic and morphological subtype. *Modern pathology : an official journal of the United States and Canadian Academy of Pathology, Inc* 28(6):845–853.
10. Weisman P et al. (2016) Genetic alterations of triple negative breast cancer by targeted next-generation sequencing and correlation with tumor morphology. *Mod Pathol* 29(5):476–488.
11. Budinska E, Bosman F, Popovici V (2016) Experiments in molecular subtype recognition based on histopathology images. (IEEE), pp. 1168–1172.
12. Zhong Q et al. (2016) Image-based computational quantification and visualization of genetic alterations and tumour heterogeneity. *Scientific Reports* 6:24146.
13. Natrajan R et al. (2016) Microenvironmental Heterogeneity Parallels Breast Cancer Progression: A Histology–Genomic Integration Analysis. *PLoS Med* 13(2):e1001961.
14. Al-Ahmadie H et al. (2011) Somatic mutation of fibroblast growth factor receptor-3 (FGFR3) defines a distinct morphological subtype of high-grade urothelial carcinoma. *The Journal of pathology* 224(2):270–279.
15. Al-Ahmadie H et al. (2016) Frequent somatic CDH1 loss-of-function mutations in plasmacytoid variant bladder cancer. *Nature genetics*.
16. Giesen C et al. (2014) Highly multiplexed imaging of tumor tissues with subcellular resolution by mass cytometry. *Nature methods* 11(4):417–422.
17. Yosinski J, Clune J, Nguyen A, Fuchs T, Lipson H (2015) Understanding Neural Networks Through Deep Visualization.
18. An J, Wang C, Deng Y, Yu L, Huang H (2014) Destruction of full-length androgen receptor by wild-type SPOP, but not prostate-cancer-associated mutants. *Cell reports* 6(4):657–669.
19. Urbinati G et al. (2016) Knocking Down TMPRSS2-ERG Fusion Oncogene by siRNA Could be an Alternative Treatment to Flutamide. *Molecular therapy. Nucleic acids* 5.
20. Schaumberg A, Sirintrapun J, Al-Ahmadie H, Schueffler P, Fuchs T (2016) DeepScope: Non-intrusive Whole Slide Saliency Annotation and Prediction from Pathologists at the Microscope.
21. Krogh A, Vedelsby J (1995) Neural network ensembles, cross validation, and active learning. *Advances in neural information processing systems* 7:231–238.
22. Sollich P, Krogh A (1996) Learning with ensembles: How over-fitting can be useful. Vol. 8, pp. 190–196.
23. Breiman L (2001) Random Forests. *Machine Learning* 45(1):5–32.
24. Jia Y et al. (2014) Caffe: Convolutional Architecture for Fast Feature Embedding.
25. Krizhevsky A, Sutskever I, Hinton G (2012) Imagenet classification with deep convolutional neural networks.
26. Cerami E et al. (2012) The cBio Cancer Genomics Portal: An Open Platform for Exploring Multidimensional Cancer Genomics Data. *Cancer Discovery* 2(5):401–404.
27. Schueffler P et al. (2013) TMARKER: A free software toolkit for histopathological cell counting and staining estimation. *Journal of pathology informatics* 4(Suppl).
28. Deng J et al. (2009) ImageNet: A large-scale hierarchical image database. (IEEE), pp. 248–255.
29. Goode A, Gilbert B, Harkes J, Jukic D, Satyanarayanan M (2013) OpenSlide: A vendor-neutral software foundation for digital pathology. *Journal of pathology informatics* 4.

Supporting Information

Algorithm S1 Preprocessing: Each patient's SPOP mutation state is paired with the whole slide image patch having the maximum number of abnormal cells, where abnormal is either cancer or unknown cell type, rather than healthy cell type. This patch is taken from the dominant tumor patch. The dominant tumor patch is both salient and has the maximum number of cancer cells. The dominant tumor patch is at low magnification, while the abnormal patch is at high magnification within the dominant.

for all *prostate adenocarcinoma patients* **do**
  $spop \leftarrow SPOP\ normal/mutated\ state\ as\ 0/1$
  $slide \leftarrow whole\ slide\ image\ of\ cancer\ biopsy$
  $patches \leftarrow 75\%\ overlap\ 800x800px\ images \leftarrow slide$
  $salient\_patches \leftarrow predict\_saliency(patches)$
  $pri\_tumor\_patch \leftarrow max\_cancer(salient\_patches)$
  $abn\_patch \leftarrow max\_abnormal(pri\_tumor\_patch)$
  if $abn\_patch < 50\%\ blurred$ **then**
    if $abn\_patch < 50\%\ background$ **then**
      if $abn\_patch < 50\%\ erythrocytes$ **then**
        if $abn\_patch\ not\ eosin\ overstained$ **then**
          $append\ (abn\_patch,\ spop)\ to\ data\_set$
return $data\_set$

Algorithm S2 Training: Train a residual network on the abnormal patch representing each patient, labeled with SPOP mutation state. The final predictor is an ensemble of eleven of such ResNets. After drawing a test set, training and validation sets are drawn from the remaining patients in the preprocessed data set (Alg S1). Within a Monte Carlo cross validation run, training and validation sets do not overlap. All draws are without replacement. Thirteen Monte Carlo cross validation runs are attempted in parallel, where training stops after eleven have validation accuracy of 0.6 or more. Some runs do not achieve 0.6 after many attempts. See Fig 5 for architecture details of $r50$ as "ResNet-50" and $drp5$ as "Drop50".

for $trial\ in\ 0, 1, 2, 3, 4$ **do**
  $test\_set \leftarrow draw(5\ SPOP\ mutants,\ 5\ SPOP\ normal)$
  for $monte\ in\ 1, 2, ..., 13\ in\ parallel$ **do**
    $train\_set \leftarrow draw(10\ mutants,\ 10\ normal)$
    $valid\_set \leftarrow draw(5\ mutants,\ 5\ normal)$
    $testable\_model \leftarrow null$
    repeat
      $r50\_model \leftarrow train\_r50(train\_set, valid\_set)$
      $drp5\_model \leftarrow train\_drp5(train\_set, valid\_set)$
      $r50\_acc \leftarrow accuracy(valid\_set, r50\_model)$
      $drp5\_acc \leftarrow accuracy(valid\_set, drp5\_model)$
      if $r50\_acc >= 0.6$ **then**
        $testable\_model \leftarrow r50\_model$
      else if $drp5\_acc >= 0.6$ **then**
        $testable\_model \leftarrow drp5\_model$
    until $11\ testable\ models$ or $testable\_model \neq null$
    $append\ testable\_model\ to\ testable\_models$
  $ensemble \leftarrow testable\_models\ with\ ensemble\ averaging$
  $ensemble\_acc \leftarrow accuracy(test\_set, ensemble)$
  $append\ ensemble\_acc\ to\ ensemble\_accs$
  $append\ ensemble\ to\ ensembles$
return $(ensembles, ensemble\_accs)$

Algorithm S3 Prediction: Use each of 5 ensembles to predict SPOP mutation state, then compute a bootstrapped CI of SPOP mutation state given these predictions. Each prediction is a probability of SPOP mutation in the patient. If the CI lower bound is > 0.5, there is significant confidence that the patient has SPOP mutation. If the CI upper bound is < 0.5, there is significant confidence that the patient does not have SPOP mutation. Otherwise, the patient's SPOP mutation state cannot be confidently predicted. Section S2 defines $P_{indep}(X|I_0, I_1, ..., I_8, C_1, C_2, ..., C_{11})$, which calculates an overall SPOP mutation prediction for the patient given the central patch, surrounding octagon of patches (Fig 6), and 11 classifiers in an ensemble.

$slide \leftarrow whole\ slide\ image\ of\ cancer\ biopsy$
$patches \leftarrow 75\%\ overlap\ 800x800px\ images \leftarrow slide$
$salient\_patches \leftarrow predict\_saliency(patches)$
$pri\_tumor\_patch \leftarrow max\_cancer(salient\_patches)$
$abn\_patch \leftarrow max\_abnormal(pri\_tumor\_patch)$
for $ensemble\ in\ ensembles$ **do**
  $I_0, I_1, ..., I_8 \leftarrow abn\_patch\ and\ surrounding\ octagon$
  $spop\_prediction \leftarrow P_{indep}(X|I_0, I_1, ..., I_8, C_1, C_2, ..., C_{11})$
  $append\ spop\_prediction\ to\ spop\_predictions$
return $confidence\_interval(spop\_predictions)$

S1. TCGA dataset learning

See Fig 7 panels A and B for MSK-IMPACT testing of the TCGA-trained metaensemble, with Fig S2 showing TCGA-trained tuned metaensemble performance. Training was as follows:

1. $P_{learn}(X = Mutant) = P_{learn}(X = Normal) = 0.5$. Each classifier is trained on twenty patients, with ten having mutant SPOP with respect to the patient germline. With this balanced dataset for training, the probability that a training example is a mutant is the same as the probability that a training example is normal, 0.5. This differs from the proportion of patients having a somatic SPOP mutation, ~10% in the TCGA dataset. Classifiers that learn on unbalanced datasets may simply learn to predict the predominant class.

2. Learning $P_{learn}(X|I, C_1, C_2, ..., C_{11})$ for each patient representative histology image I and eleven classifiers C. This learns the probability that a classifier will predict the patient is mutated, given the representative histology image of the patient. An ensemble of an infinite number of classifiers would give the expected value of this probability. We use eleven classifiers. Each classifier tends to emit either a zero or one, predicting mutant or normal, i.e. $P_{learn}(X|I, C)$ tends to be 0 or 1. We take the ensemble average to be the probability P_{learn}, which tends to be uniformly distributed rather than bimodal (Fig S1): $P_{learn} = P_{learn}(X|I, C_1, C_2, ..., C_{11}) = (1/11) * \sum_{i=1}^{11} P_{learn}(X|I, C_i)$.

3. Training and validation sets consist of a central image patch and eight surrounding image patches in an octagon formation (Fig 6), where the distance between the central patch and a surrounding patch is the same as the distance between any two adjacent surrounding patches. All patches had the same label, either 1 for patients with somatic SPOP mutation or 0 for paients without somatic SPOP mutation. This approximately circular region of nine patches per patient both provides more information for training and more closely resembles the region available from a circle of tissue in a TMA.

4. The test set consists of a single patch per patient, without a surrounding octagon of eight patches. Test accuracy and squared loss were optimized from the converged trained models having at least 0.6 validation accuracy, i.e. the "sel" ensembles in Fig S2. This optimization selected at most one model from 11 of 13 Monte Carlo cross validation runs, where the selection of 11 models for the ensemble had the highest accuracy and lowest squared loss on the test set. This ensures on unseen data the ensemble has both the discriminative power and diversity to correctly predict P_{learn}, a function of a single image.

S2. MSK-IMPACT dataset testing

See Fig 7 panel C for MSK-IMPACT testing of the TCGA-trained metaensemble. Testing was as follows:

1. $9 * P_{indep}(X = Mutant) \approx P_{indep}(X = Normal)$. The ensembles learned on the TCGA dataset are tested on an independent MSK-IMPACT dataset 152 patients, 19 having somatic SPOP mutation, so the probability that one of these MSK-IMPACTed patients is mutated is only ~10%. This is in sharp contrast to the TCGA training set, where the probabilities of mutant and wild type patients are equal, due to the stratified sampling for training. Because $P_{learn}(X = mutant) = 0.5$ is greater than $P_{indep}(X = mutant) \approx 0.1$, additional scaling or stringency is required to avoid false positives from the learned classifier applied to the independent dataset.

2. Evaluating $P_{indep}(X|I_0, I_1, ...I_8, C_1, C_2, ..., C_{11})$ for each patient. Each of the eleven classifiers are evaluated on the patient's central representative histology image and the octagon of eight surrounding images (Fig 6), to predict SPOP mutation. Because each classifier has been trained on only 10 mutants and 10 non-mutants, many classifiers will emit a biased prediction of 0 for all nine images or 1 for all nine images, lacking power to discriminate among the nine images. Empirically however, 1-3 classifiers tend to have greater variance in their predictions for each of the nine images of the patient. The classifiers with greater variance tend to correctly predict SPOP mutation state, presumably because the features learned from similar training data can distinguish image regions showing mutant image textures from regions showing non-mutant image textures. Such mutant and non-mutant regions should spatially cluster, i.e. a classifier should make the same SPOP mutation state prediction for adjacent images in a patient, otherwise the classifier is predicting noise. If, for instance, a classifier predicts SPOP is mutated in each of 4 adjacent images, there is significant evidence for SPOP mutation at $\alpha = 0.05$: of 9 images, 16 possibilities exist of 4 adjacent images being SPOP mutants and the other images being non-mutants, and $2^9 = 512$ mutant/non-mutant configurations possible, so probability of 4 adjacent images is $16/512 = 0.03125 < 0.05 = \alpha$. Thus for added stringency, one may take as the corrected P_{indep} the maximum of all adjacent 4-image cluster prediction minima. $P_{indep4} = \max(\min_{i \in a,b,c,d}(P_{learn}(X|I_i, C)))$. However, due to the noisy nature of the predictions from classifiers trained on little data, a mutant 4-cluster may not occur, but additional adjacent images indicating mutation may offer supporting evidence. From the observation that a 4-cluster is two overlapping 3-clusters, we slightly loosen the correction stringency to $P_{indep3pen}(X|I_0, I_1, ...I_8, C) = pen(\min(P_{learn}(X|I_a, C), P_{learn}(X|I_b, C), P_{learn}(X|I_c, C)))$, $\forall\{I_a, I_b, I_c\} \in \{I_0, I_1, ..., I_8\}$ $s.t. (I_a \; adjacent \; I_b) \; and \; (I_b \; adjacent \; I_c)$, where $pen(...)$ returns the second-greatest value, or penultimate. In this way, $P_{indep3pen}$ is identical to P_{indep4} for a 4-cluster, but additionally allows partially- or non-overlapping 3-clusters to suggest SPOP mutation. $P_{indep3pen}$ is strictly greater than or equal to P_{indep4}. Finally, the $P_{indep3pen}$ from a classifier with greater variance of all nine image predictions in the patient should be weighted higher, due to our lesion hypothesis of localized SPOP-mutation-driven slide pathology (and greater accuracy of such a classifier in practice compared to that from a different classifier with lesser variance, e.g. predicting all 0 or all 1 on the same images). The weighted ensemble average is then $P_{indep}(X|I_0, I_1, ..., I_8, C_1, C_2, ..., C_{11}) = (\sum_{i=1}^{11}(Var_i * P_{indep3pen}(X|I_0, I_1, ..., I_8, C_i)))/\sum_{i=1}^{11} Var_i$, where we define $Var_i = (\sum_{j=0}^{8}(P_{learn}(X|I_j, C_i) - \mu_i)^2) + \frac{(1-\mu_i)^2 + (0-\mu_i)^2}{8}$ and $\mu_i = (1/11)\sum_{k=1}^{11} P_{learn}(X|I_k, C_i)$, so that even classifiers that predict 0 for all images or 1 for all images still have some small weight.

S3. Implementation Details

We studied a TCGA cohort of 499 prostate adenocarcinoma patients, in particular the 177 patients that had both acceptable pathology images and SPOP mutation state available (Fig 1, Alg S1). SPOP mutation state was downloaded from cBioPortal [26]. After learning on TCGA data, we tested on an MSK-IMPACT dataset of 19 SPOP mutant patients and 119 wild type patients.

Microscope slides were scanned at 0.25 ± 0.003 microns per pixel [μpp], using an Aperio AT2 scanner. The resulting SVS data file consists of multiple levels, where level 0 is not downsampled, level 1 is downsampled by a factor of 4, level 2 by a factor of 16, and level 3 by a factor of 32. From each level, 800x800px patches were extracted via the OpenSlide software library [29]. We refer to level 2 as low magnification and level 0 as high magnification. Level 2 approximately corresponds to a 10x eyepiece lens and 10x objective lens at the microscope when the scan is $0.5\mu pp$. Our saliency predictor assumed $0.5\mu pp$ scans, though the scans here were $0.25\mu pp$, but appeared robust.

Algorithm S1 describes data preprocessing for training. In prior work, we developed a patch saliency predictor [20]. A TMARKER classifier was trained to determine cell types [27]. We define the dominant tumor patch as having the maximum number of cancer cells of all 800x800px salient patches at low magnification. Within the 800x800px dominant tumor patch, we select an 800x800px patch at high magnification having the maximum number of abnormal cells. Malignant cells count 1 towards the maximum abnormal cell count, unknown cells count 0.5, and healthy cells count 0. The

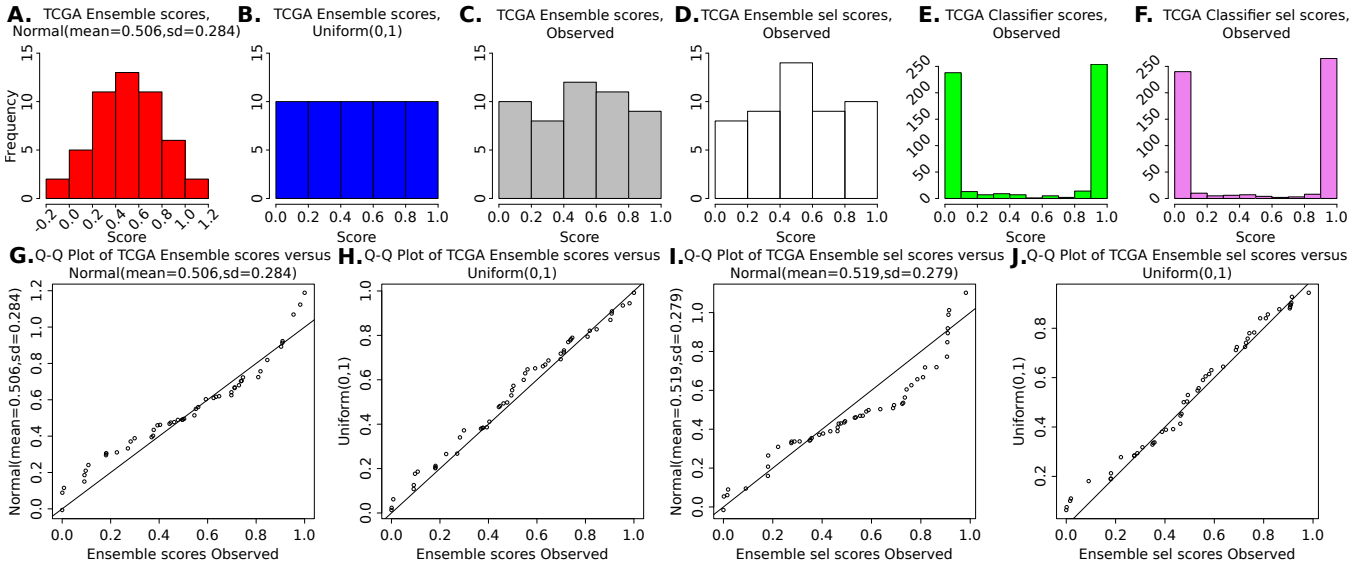

Fig. S1. TCGA classifier and ensemble mutation prediction scores, showing ensemble scores are uniform random variables representing the mutation probability when the mutant and non-mutant classes are equally sampled, despite the sharply bimodal score distribution of individual classifiers (Table S1). This uniform random distribution enables valid confidence interval calculation over ensemble mutation prediction scores without confounds such as p-value inflation, e.g. a disproportionate number of ensemble mutation prediction scores being close to zero. **Panel A:** Normal distribution of scores with mean and stdev of TCGA-trained ensemble prediction scores, showing the distribution domain extends beyond the valid [0,1] domain of mutation prediction scores. **Panel B:** Uniform distribution of scores. **Panel C:** TCGA-trained ensemble scores, following Unfiform distribution (KS Test p=0.9977). Corresponds to Fig 4 panel A, second from right. **Panel D:** TCGA-trained tuned ensemble scores, following a Uniform distribution (KS Test p=0.7202). Corresponds to Fig 4 panel A, far right. The excess of predictions around 0.5 is an artifact of the tuning process, which tends to select classifiers for the ensemble such that the ensemble prediction is at least 0.5 for mutants and less than 0.5 for non-mutants if the ensemble prediction was incorrect before tuning. See also Fig S2 for tuned ensemble performance. **Panel E:** TCGA-trained classifier scores, following sharply bimodal distribution of 0 (non-mutant) or 1 (mutant) predictions. far right. **Panel F:** TCGA-trained classifiers selected for the tuned ensemble are also bimodal. **Panel G:** Q-Q plot showing outliers, indicating TCGA-trained ensemble scores do closely follow a Normal distribution. **Panel H:** Q-Q plot showing close linear relationship, indicating TCGA-trained ensemble scores follow a Uniform distribution. **Panel I:** Q-Q plot showing outliers, indicating TCGA-trained tuned ensemble scores do not closely follow a Normal distribution. **Panel J:** Q-Q plot showing close linear relationship, indicating TCGA-trained tuned ensemble scores follow a Uniform distribution.

dominant tumor is explored in increments of 10 pixels, until the bounding box with the maximum number of abnormal cells is found. Whereas our saliency predictor operated on low-power tissue-level details of a patch, our SPOP predictor operates on high-power cell-level details of a patch. A patient is discarded from the study if the abnormal patch over-stained eosin blue, or is $> 50\%$ blurred, or is $> 50\%$ background, or is $> 50\%$ blood – as determined by visual inspection.

Algorithm S2 describes the neural network ensemble for training. This procedure allows learning to occur despite a mere 20 patients having an SPOP mutation, compared to 157 not having an SPOP mutation. Additionally, having 5 ensembles – each trial yielding one ensemble of 11 ResNets – allows a CI in predicted SPOP mutation state to be calculated for both the generalization error estimate during training and any future patient (Algorithm S3). Moreover, such a large number of ResNets can fully sample the SPOP wild type patients, while each ResNet is still trained with an equal proportion of SPOP mutants and wild types. We use two neural network architectures, both the published ResNet-50 architecture ($r50$ in Alg S2) and our custom ResNet-50 with a 50% dropout [4] layer with an additional 1024 fully-connected layer as the top layer ($drp5$ in S2, and shown as Drop50 in Fig 5). In practice, at least one architecture tended to have validation accuracy ≥ 0.6. Architecture diversity may increase intra-ensemble ResNet variance, and the decorrelation in errors should average out in the ensemble. Trials 0, 2, and 3 used two Drop50 learners and nine ResNet-50 classifiers (Fig 5, Table S1). Trial 1 had six and five, respectively. Trial 4 had three and eight. Trials 1 and 4 had the worst performance by AUROC (Fig 7), both had at least one ResNet-50 predictor with 0.3 or worse test set accuracy (Table S1), and both had more than two Drop50 learners in the final ensemble for the trial. For challenging draws of training, validation, and test sets, Drop50 learners may slightly outperform ResNet-50 learners, though generalization accuracy may remain low due to the clustering of the data in the draws and limited sample sizes.

ResNets (both ResNet-50 and Drop50 architectures) were trained on 10 mutant and 10 non-mutant patients, so with data augmentation each ResNet was trained on 21600 images total. For each training set, a validation set of 5 mutant and 5 non-mutant patients was used and did not overlap with the training set, so with data augmentation each ResNet was validated against 10800 images. The test set for an ensemble consistent of 5 mutant and 5 non-mutant patients which were not augmented and did not overlap with any training or validation set for any classifier in the ensemble, so each ensemble was tested against 10 images.

There is remarkable variability in test accuracy among the testable models from each Monte Carlo cross validation run (Table S1). If the test set is drawn from approximately the same distribution as the validation set, where ResNet validation accuracy is 0.6+ and ResNets are uncorrelated, then we can expect 6 of the 11 ResNets ($6/11 < 0.6$) in an ensemble to correctly predict SPOP mutation state on average. In this way the ensemble is a strong learner based on ResNet weak learners [21, 22]. Through ensemble averaging, the mean SPOP mutation probability is computed over all 11 constituent ResNets, to provide the final probability from the ensemble.

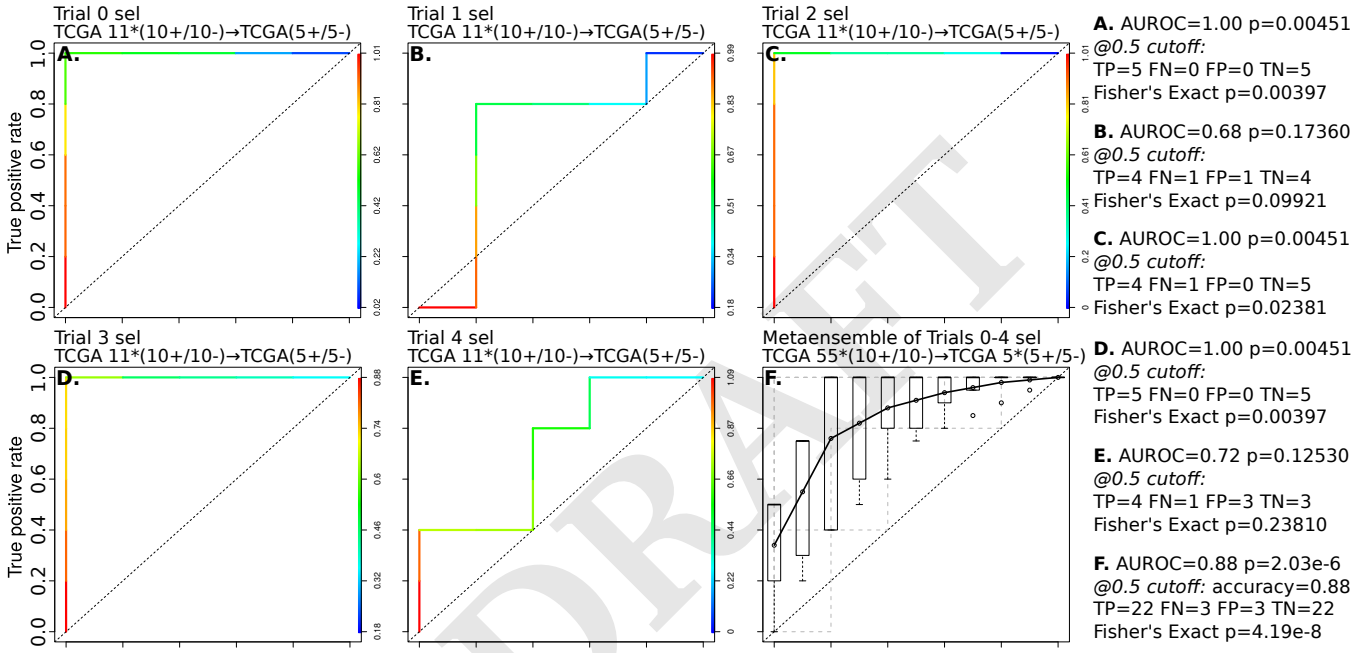

Fig. S2. Tuned ensemble performance, for comparison to ensemble performance in Fig 4 panel B. The tuned ensembles are used for prediction on the independent MSK-IMPACT cohort (Fig 4 panel C). Tuning provides limited additional training for each ensemble via model selection on the corresponding TCGA test set. Tuned ensemble mutation prediction distributions shown in Fig S1.

Table S1. TCGA test set images and accuracies, with prediction errors from single residual networks highlighted in red and prediction errors from residual network ensembles highlighted in magenta. New 20-patient training and 10-patient validation sets are drawn for each Monte Carlo cross validation run against the trial's 10-patient test set. The far right column is used to calculate the mean classifier prediction, which is used as the trial's ensemble prediction. The five ensemble predictions are used to calculate a confidence interval of generalization accuracy, shown in Fig 4 panel A second from right in gray and red. Individual classifier predictions follow a sharply bimodal distribution of 0 (non-mutant) or 1 (mutant), while the ensemble predictions follow a uniform random distribution (Fig S1).

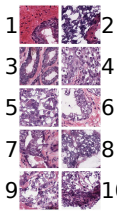

Trial0 Test # :	SPOP	Monte1	Monte2	Monte3	Monte4	Monte5	Monte6	Monte7	Monte8	Monte9	Monte10	Monte11	Mean
1 : 0	0.0000	0.0000	0.0000	0.0000	0.0000	0.0000	0.0000	0.9988	0.0000	0.0000	0.9987	0.1816
2 : 1	1.0000	1.0000	1.0000	0.8637	0.0613	1.0000	0.1741	0.1386	1.0000	1.0000	0.9647	0.7457
3 : 0	0.0000	0.0000	0.0000	0.0000	0.0000	0.0001	0.0000	1.0000	0.0000	0.9892	0.0000	0.1808
4 : 1	0.3284	0.0000	0.0000	0.7208	1.0000	1.0000	1.0000	1.0000	1.0000	0.9691	1.0000	0.7289
5 : 0	1.0000	0.0006	0.0001	0.0020	1.0000	1.0000	1.0000	1.0000	0.9845	0.0001	0.0114	0.5453
6 : 1	0.0124	1.0000	0.9970	0.2412	0.9999	0.9982	0.0000	0.0001	0.0017	0.0000	0.9990	0.4772
7 : 0	0.0000	0.0000	0.0000	0.0000	0.0000	0.0750	0.0000	0.9931	0.0001	0.0000	0.0000	0.0971
8 : 1	0.1069	1.0000	0.9992	0.8635	0.0054	1.0000	0.9991	1.0000	0.6994	0.9997	0.0036	0.6979
9 : 0	0.9990	0.0156	0.9989	0.0005	0.9978	0.9844	1.0000	0.1079	0.4288	0.0000	0.0000	0.5030
10 : 1	0.0013	0.2339	0.9962	0.0001	0.9978	0.0000	1.0000	1.0000	0.8206	0.9975	0.0197	0.5516

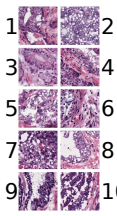

Trial1 Test # :	SPOP	Monte1	Monte2	Monte3	Monte4	Monte5	Monte6	Monte7	Monte8	Monte9	Monte10	Monte11	Mean
1 : 0	0.1674	0.0007	0.0041	0.0005	0.6145	0.0001	0.0002	0.0016	0.3730	0.9999	0.0000	0.1813
2 : 1	0.9580	1.0000	1.0000	1.0000	1.0000	1.0000	0.9973	1.0000	1.0000	1.0000	1.0000	0.9542
3 : 0	0.0839	0.0000	0.0001	0.0000	0.0000	0.0048	0.0000	0.0022	0.0000	1.0000	0.0000	0.0916
4 : 1	0.0845	0.0000	0.0000	0.0000	0.0008	0.0000	0.0000	0.0114	0.0000	1.0000	0.0000	0.0920
5 : 0	0.6265	0.9999	1.0000	0.9998	0.9747	0.9933	0.0001	1.0000	0.0000	0.3829	0.1641	0.5925
6 : 1	0.4271	0.1278	1.0000	0.0008	0.0010	0.0000	0.0000	1.0000	0.8001	1.0000	0.0003	0.3750
7 : 0	1.0000	1.0000	1.0000	1.0000	1.0000	1.0000	1.0000	1.0000	1.0000	1.0000	1.0000	1.0000
8 : 1	0.4438	0.0000	1.0000	0.0002	0.4147	0.0000	0.9095	0.0011	1.0000	1.0000	0.0000	0.3932
9 : 0	0.4236	0.0000	0.3012	0.0004	1.0000	0.9998	0.0000	0.0001	0.8132	1.0000	0.0000	0.4621
10 : 1	0.8278	0.9999	1.0000	1.0000	1.0000	0.9312	1.0000	1.0000	0.9999	0.9729	1.0000	0.9030

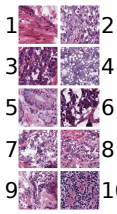

Trial2 Test # :	SPOP	Monte1	Monte2	Monte3	Monte4	Monte5	Monte6	Monte7	Monte8	Monte9	Monte10	Monte11	Mean
1 : 0	0.0744	0.0000	0.0000	0.0000	0.0000	0.0000	0.0002	0.0001	0.0000	0.0000	0.0077	0.0075
2 : 1	0.9993	0.0022	0.9999	0.1242	1.0000	0.0000	0.0412	1.0000	0.9674	0.9995	0.9880	0.6474
3 : 0	0.2742	0.0000	0.8778	0.0000	1.0000	0.0044	1.0000	0.1288	0.0040	0.0000	0.0000	0.2990
4 : 1	1.0000	0.9989	1.0000	1.0000	1.0000	1.0000	1.0000	1.0000	1.0000	0.0008	1.0000	0.9091
5 : 0	0.0000	0.0057	0.0000	0.0000	0.0000	0.0000	0.0000	0.0019	0.0002	0.0000	0.0000	0.0007
6 : 1	0.9904	0.0003	1.0000	1.0000	1.0000	1.0000	0.9994	1.0000	1.0000	1.0000	1.0000	0.9082
7 : 0	0.9971	0.0002	0.0001	0.9961	1.0000	0.0000	0.9309	0.0000	0.0000	0.0019	0.9975	0.4476
8 : 1	0.9968	0.0001	0.2478	0.0057	1.0000	0.0000	1.0000	0.0037	0.0000	0.9858	0.2014	0.4038
9 : 0	0.9628	0.4937	0.3145	0.0126	0.9987	0.6667	0.0002	0.0721	0.0000	0.0000	0.6324	0.3776
10 : 1	1.0000	0.0000	1.0000	0.7263	1.0000	1.0000	0.9654	1.0000	0.0043	1.0000	0.4465	0.7402

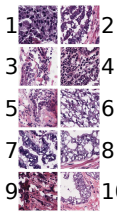

Trial3 Test # :	SPOP	Monte1	Monte2	Monte3	Monte4	Monte5	Monte6	Monte7	Monte8	Monte9	Monte10	Monte11	Mean
1 : 0	0.9820	0.0000	0.0000	0.0000	0.9999	0.0000	0.0000	0.0000	0.0000	0.0000	1.0000	0.2711
2 : 1	0.0703	0.3796	0.0034	1.0000	0.0007	1.0000	1.0000	0.0000	0.9955	0.9872	0.0364	0.4976
3 : 0	0.9994	1.0000	0.1613	0.0000	0.9959	0.2808	1.0000	1.0000	0.0010	0.0003	0.0000	0.4944
4 : 1	1.0000	0.0002	1.0000	0.3774	0.9294	1.0000	1.0000	1.0000	1.0000	1.0000	1.0000	0.8461
5 : 0	0.0000	0.0419	0.0016	0.0009	0.0000	1.0000	1.0000	1.0000	0.0003	0.8270	1.0000	0.4429
6 : 1	1.0000	1.0000	0.0104	1.0000	1.0000	1.0000	1.0000	0.0989	1.0000	1.0000	0.0011	0.7373
7 : 0	0.0688	0.9645	0.0434	1.0000	0.0000	0.0000	0.0000	0.0000	1.0000	0.9813	0.0009	0.3690
8 : 1	0.9998	1.0000	0.8986	1.0000	1.0000	1.0000	1.0000	0.9981	1.0000	0.0004	0.0000	0.8088
9 : 0	0.0002	0.0147	1.0000	0.0000	0.5648	0.0002	0.0000	0.0000	0.0006	0.0000	0.9010	0.2256
10 : 1	0.0000	1.0000	0.0003	0.9888	0.8783	0.0040	1.0000	1.0000	1.0000	0.9989	0.0000	0.6246

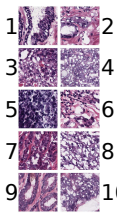

Trial4 Test #:	SPOP	Monte1	Monte2	Monte3	Monte4	Monte5	Monte6	Monte7	Monte8	Monte9	Monte10	Monte11	Mean
1 : 0	1.0000	0.0167	1.0000	0.9963	1.0000	0.9630	0.8542	0.0000	0.0011	0.9922	1.0000	0.7112
2 : 1	0.0000	0.0001	0.0000	0.0000	0.0086	0.9996	0.0001	0.0073	0.1754	0.0000	0.0001	0.1083
3 : 0	1.0000	1.0000	1.0000	0.9972	0.0000	1.0000	0.9999	1.0000	1.0000	1.0000	0.0003	0.8179
4 : 1	0.3789	1.0000	0.3241	0.0000	0.9964	1.0000	1.0000	0.9993	1.0000	0.9718	0.0078	0.6980
5 : 0	0.0000	0.9928	0.9998	0.8345	0.0000	1.0000	0.9999	0.0000	0.9993	1.0000	0.9997	0.7115
6 : 1	0.0039	1.0000	1.0000	0.9746	0.9988	0.9970	0.0001	0.0000	0.0038	1.0000	0.9988	0.6343
7 : 0	0.0000	0.0065	0.0000	0.1120	0.0000	1.0000	0.9833	1.0000	0.0000	0.0000	0.0057	0.2825
8 : 1	1.0000	1.0000	1.0000	1.0000	0.9983	1.0000	1.0000	1.0000	0.8101	1.0000	0.9926	0.9819
9 : 0	0.0000	0.0000	0.0000	0.0000	0.0000	0.0000	0.0000	0.0000	0.0000	0.0000	0.0000	0.0000
10 : 1	0.1585	0.9483	0.2321	0.8237	0.9974	1.0000	1.0000	0.0000	1.0000	0.0134	0.0000	0.5612